1st Revision

Long-term stability of avalanche scaling and integrative network organization in prefrontal and premotor cortex

Stephanie R. Miller[1], Shan Yu[1,2], Sinisa Pajevic[3], and Dietmar Plenz[1]

[1] Section on Critical Brain Dynamics, National Institute of Mental Health, Bethesda, MD, USA.

[2]Current address: Brainnetome Center, Institute of Automation, Chinese Academy of Sciences, China.

[3]Section on Quantitative Imaging and Tissue Sciences, National Institute of Child Health and Development, NIH, Bethesda, MD, USA.

Pages/Figures: 6 figures, 4 tables

Running Head: Long-term stability in avalanches and integrative networks

Correspondence: Dietmar Plenz, Ph.D., Section on Critical Brain Dynamics, National Institute of Mental Health, Porter Neuroscience Research Center, Rm 3A-1000, 35 Convent Drive, Bethesda, MD 20892, (301) 402-2249 office, (301) 480-7480 fax, plenzd@mail.nih.gov

Keywords: nonhuman primate, resting activity, criticality, brain dynamics, neuronal avalanches, integrative network organization

Abstract

Ongoing neuronal activity in the cortex establishes functional networks of synchronization that reflect normal and pathological brain function. The reconstruction of these networks typically suffers from the use of indirect measures of neuronal activity at low spatiotemporal resolution and a lack of longitudinal tracking. Accordingly, the precise nature of the underlying synchronization dynamics and its translation into robust graph theoretical markers are not well characterized. Here, we studied the stability of cortical dynamics and reconstructed functional networks over many weeks in prefrontal and premotor cortex of awake nonhuman primates. We monitored neuronal population activity directly in the ongoing local field potential (LFP) at high spatial and temporal resolution using chronically implanted high-density microelectrode arrays. Ongoing activity was composed of neuronal avalanches exhibiting stable, inverted parabolic profiles with the collapse exponent of 2 in line with a critical branching process. Avalanche-based functional networks, reconstructed using a Normalized Count estimator, revealed robust integrative properties characterized by high neighborhood overlap between strongly connected nodes and robustness to weak-link pruning. “Entropy of mixing” analysis demonstrated progressive link reorganization over weeks. The long-term stability of avalanche scaling and integrative network organization should support the development of robust biomarkers to characterize normal and abnormal brain function.

Introduction

Ongoing neuronal activity in the mammalian brain gives rise to distinct functional networks that reflect normal and pathological brain function (Bullmore and Sporns, 2009; Fox and Raichle, 2007; Raichle, 2015). Empirical measures of these networks, however, are often limited in the precision with which they reflect the organization of neuronal population activity and a lack of longitudinal follow-up. Networks are either reconstructed from indirect non-neuronal activity at low temporal resolution using functional magnetic resonance imaging (fMRI), or via more direct neuronal activity measures such as magnetoencephalography (MEG) and the electroencephalogram (EEG) which suffer predominantly from low spatial resolution (Bassett and Sporns, 2017). Accordingly, there is limited knowledge about the stability and nature of the spatiotemporal dynamics and corresponding functional connectivity of local neuronal populations that give rise to fluctuations in ongoing cortical activity.

In contrast to macroscopic and indirect methods, neuronal activity measured at single-cell resolution could in principle allow for precise and robust spatiotemporal reconstruction of functional networks in cortex. For example, in macaque cortex single-unit activity can be recorded over many weeks (Nicolelis et al., 2003) and identifies firing statistics of neurons over days (Dickey et al., 2009; Jackson and Fetz, 2007). Advanced approaches may involve tetrodes, automated classifiers (Tolias et al., 2007) or second order statistics as classifiers (Fraser and Schwartz, 2011). Even advanced single-unit approaches, however, limit robust tracking of activity to small groups of individual neurons. Chronic expression of genetically-encoded calcium indicators (GECIs) can increase the neuronal count and identify orientation-selective neurons over months (Li et al., 2017), yet at low temporal resolution. The local field potential (LFP), alternatively, provides access to an intermediate spatial resolution of cortical activity that

is between the macroscopic scale of fMRI, MEG and EEG and single cell accuracy. It robustly measures local neuronal population activity with high temporal and reasonable spatial resolution of several hundred micrometers (e.g. (Bellay et al., 2021; Katzner et al., 2009)) over many weeks. In nonhuman primates (NHPs), the LFP has been shown to correlate well with local unit-activity (Donoghue et al., 1998; Petermann et al., 2009; Rasch et al., 2008) and offers robust brain-machine interface performance (Mehring et al., 2003).

It is now well established that the ongoing LFP in superficial layers of nonhuman primates organizes into spatiotemporal activity clusters whose sizes and durations distribute according to power laws (Miller et al., 2019; Shew et al., 2009; Yu et al., 2017), the hallmark of neuronal avalanches (Beggs and Plenz, 2003). The spatiotemporal correlations underlying neuronal avalanches give rise to functional "integrative" networks, in which the topology and weights of links organize such that end-nodes of strong links are more likely to have many common neighbors, as quantified by a high correlation between the link weight and the link clustering coefficient ((Pajevic and Plenz, 2012), *cf.* edge-clustering coefficient in (Radicchi et al., 2004)), while being robust to the loss of weak links, in terms of maintaining the advantages of a small-world topology (Watts and Strogatz, 1998). This specific arrangement describes many complex networks ranging from genetic networks to social, i.e. "friendship", networks (Pajevic and Plenz, 2012). Importantly, integrative networks can form using local plasticity rules that operate on neuronal avalanches (Alstott et al., 2015) in which weak links provide a large basin for plastic changes as they can be removed or rewired, permitting flexibility, while preserving the small-world network property. The stability over days and weeks of cortical avalanche dynamics and corresponding integrative networks has not been explored for cortex. Size and duration distributions of avalanches do not consider the spatiotemporal organization of

avalanches, thus multiple functional connectivities could give rise to similar power law statistics. Likewise, integrative networks allow for the reorganization of individual links while maintaining global integrative properties (Pajevic and Plenz, 2012).

Here we recorded ongoing LFP activity in prefrontal and premotor cortex of NHPs over weeks using chronically implanted high-density microelectrode arrays. We demonstrate stable avalanche dynamics with power law statistics, the temporal avalanche profile of an inverted parabola and corresponding scaling exponent of 2, which is the expected value for critical branching process dynamics (di Santo et al., 2017; Miller et al., 2019; Sethna et al., 2001). We further demonstrate that these avalanches give rise to non-trivial integrative functional networks despite progressive reorganization of the link strengths as identified using Normalized Count (NC) estimators (Pajevic and Plenz, 2009) and the "entropy of mixing" analysis (see Material and Methods). Our results suggest that avalanche dynamics and corresponding integrative network organization identify a robust cortical state in the adult brain, which should inform dynamical models of brain function and might allow for the early identification of pathological brain states.

Results

The spatiotemporal organization of the ongoing LFP (1 – 100 Hz) was monitored with chronically implanted high-density microelectrode arrays (~10 x 10 electrodes; interelectrode distance 400 μm) in premotor (PM, n = 2 arrays) and prefrontal cortex (PF, n = 4 arrays) of three macaque monkeys (*Macaca mulatta*; K, V, N; Fig. 1A, B). The animals were awake and seated in a monkey chair during the recording sessions but were not given any specific stimulus or task.

86

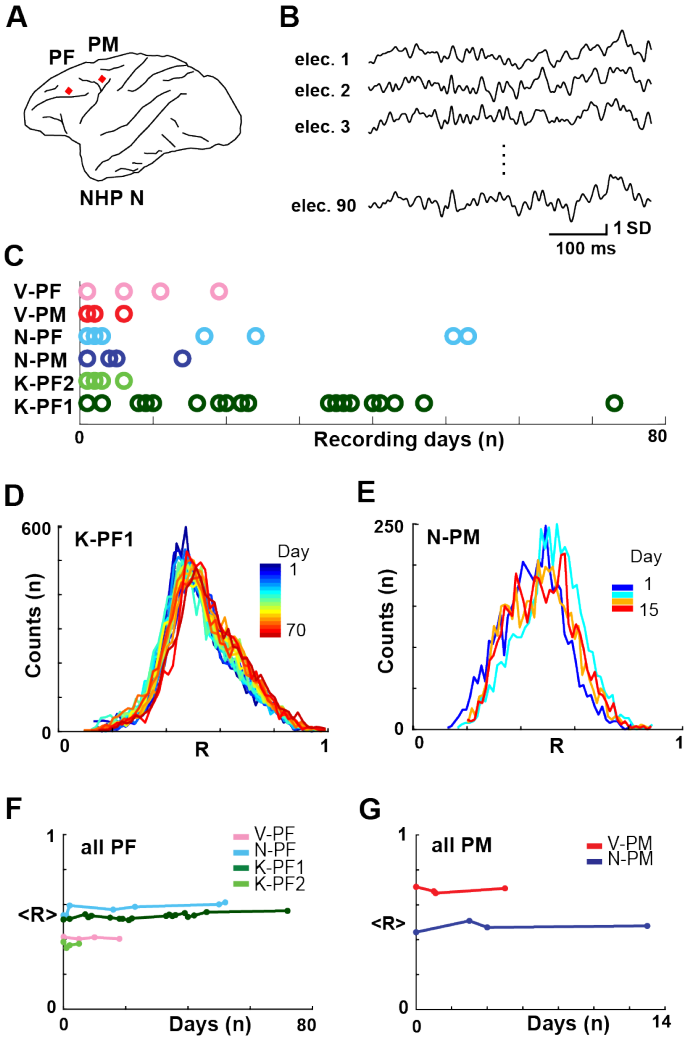

Figure 1: Ongoing cortical dynamics are stable over weeks in superficial layers assessed by pairwise correlations in the LFP. A, Sketch of chronic prefrontal (*PF*) and premotor (*PM*) cortical implantation sites (*red diamonds*) for high-density microelectrode arrays. **B,** Example of simultaneously recorded ongoing LFP (1 – 100 Hz) at single electrodes with correlated activity. **C,** Overview of ~30 min recording sessions per day (*color coded circles*) over several weeks for each NHP. **D, E,** Pair-wise correlations of the continuous LFP distribute similar over time. Normalized histogram of pairwise correlations between all functioning channels for each recording day (*color bar*) in two NHPs (*left*: prefrontal recording in K; *right*: premotor recordings in N). **F, G**, The average correlation, <*R*> (from *D*, *E*), was constant over weeks in PF (*left*) and PM (*right*) arrays.

On average about 4 ± 2 hr of LFP activity during 9 ± 7 recording sessions over the course of 5 ± 4 weeks were analyzed per monkey (85 ± 8 electrodes/array; Fig. 1C).

Stability of average pairwise correlation and avalanche dynamics in prefrontal and premotor cortex

The pairwise Pearson's correlation, R, is a standard measure to quantify the correlation in neuronal activity between distant cortical sites. We found that for the continuous LFP, the distribution of R, obtained from ~5,000 electrode comparisons per array, was broad yet similar across days (Fig. 1D, E). The average correlation, $\langle R \rangle$, while different between arrays, was constant over many days and weeks (Fig. 1F, G; linear regression fit of $0.4 \pm 0.7 \times 10^{-2}$ for all arrays; see Table 1 for individual arrays).

We next explored the stability of neuronal avalanche dynamics by discretizing the LFP from ongoing activity in the NHPs (Petermann et al., 2009; Yu et al., 2017). We previously demonstrated that negative deflections in the continuous LFP signal (nLFPs) track the local neuronal population activity and correlate with extracellular unit firing (Bellay et al., 2021; Petermann et al., 2009). Accordingly, discrete nLFPs were defined by crossing a threshold of -2 SD and extracting their peak times (Fig. 2A). nLFPs were then grouped into avalanches at temporal resolution Δt of the mean time interval of successive nLFPs on the full array, $\langle IEI \rangle$, which ranged between 3 – 4 ms (Fig. 2B; see Material and Methods). We found that the probability density distribution of avalanche size, which typically ranges from size 1 to the number of electrodes for each array (Yu et al., 2011), exhibited power laws for each day of recording (Fig. 2C, D; $\Delta t = \langle IEI \rangle$, truncated power law vs. exponential, LLR >> 1, $p < 0.005$; or vs. log-normal, LLR>>1, $p < 0.005$; constant across all recording days). The stability of the

109

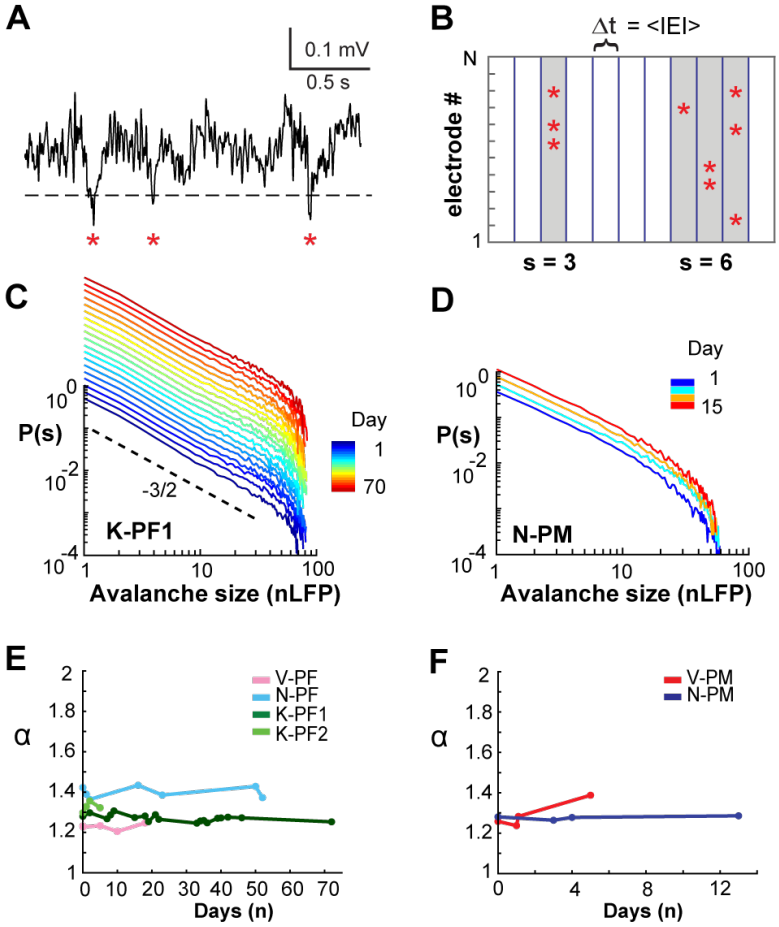

Figure 2: Neuronal avalanche dynamics is stable over weeks in frontal cortex of NHPs. A, Sample ongoing LFP at single electrode. A negative threshold (*dashed line*) is applied to identify significant negative deflections from the mean (nLFPs, *red asterisks*). **B,** Schematic nLFP raster at Δt = ⟨IEI⟩ showing neuronal avalanches identified as concurrent or consecutive nLFPs on the array separated by at least one empty time bin. Two avalanches (*gray*) of size 3 and 6 are identified. **C, D,** Power law in size S for nLFP avalanches for all recordings (*color bar*) in two NHP (Δt = ⟨IEI⟩). *Broken line*: power law with slope -3/2 as visual guide. *Color bar*: Recording day. Size distributions remain power laws for all days (LLR values > 0 significant; vs. exponential distribution; see also Table 1). **E, F,** Stability of slope α as a function of time (*color coded*).

power law in size was associated with an average slope $\alpha = 1.32 \pm 0.05$ for all arrays (Table 1), which is close to the expectations for the size exponent of a critical branching process (Fig. 2E, F) (Harris, 1963). These results demonstrate the presence of avalanche dynamics in all NHPs for up to 2 weeks in PM and up to 10 weeks in PF.

Long-term stability in the temporal profile of avalanches and corresponding scaling collapse

The temporal profile of a neuronal avalanche describes how avalanches unfold in time by initiating locally, growing in magnitude, and eventually contracting spatially before ending. Recent work (Miller et al., 2019) confirmed the prediction that the temporal profile of neuronal avalanches obeys the characteristic motif of an inverted parabola and that empirically-observed mean avalanche profiles collapse onto this scale-invariant motif regardless of avalanche duration. For this analysis, the temporal resolutions were set to $\Delta t = 1$ ms and $\Delta t = 30$ ms respectively, which demonstrated stable power law size distributions and expected change in slope α (Table 1; 1 ms: all LLR > 10^4, all $p << 0.005$; 30 ms: all LLR > 10, all $p << 0.005$) as reported previously (Beggs and Plenz, 2003; Petermann et al., 2009). These resolutions allow for the collapse of temporal avalanche profiles in the presence of transient γ–oscillations in ongoing PF and PM activity of NHPs (Miller et al., 2019).

We explored the stability of these scaling predictions over time, finding that the characteristic motif for mean profiles of avalanche lifetime, L, with $L = 3\Delta t - 5\Delta t$ did trace inverted parabolas for fine ($\Delta t = 1$ ms, Fig. 3A, B,) and coarse ($\Delta t = 30$ ms, Fig. 3C, D) temporal resolutions (for statistical comparison see Table 2 for individual arrays). Importantly, the scaling exponent χ producing these parabolic, collapsed motifs was close to the value of 2 expected for a critical branching process (di Santo et al., 2017; Miller et al., 2019; Sethna et al., 2001) and did

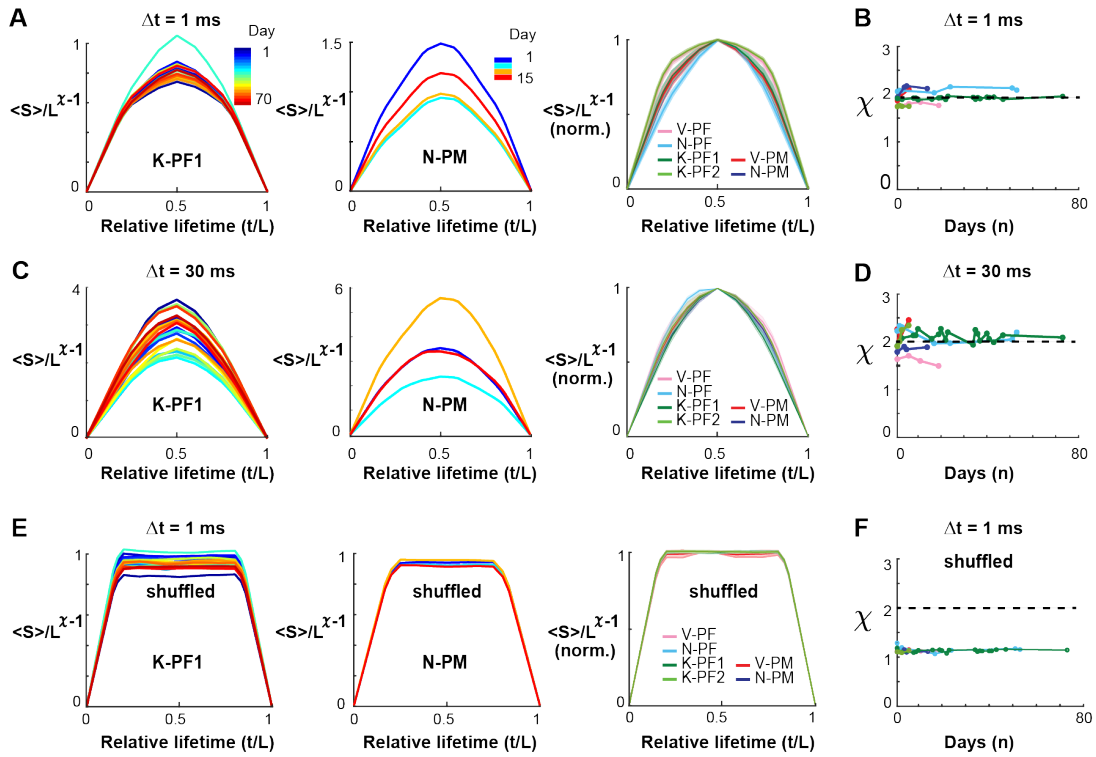

Figure 3: Collapse in the temporal profiles of neuronal avalanches and corresponding scaling exponent χ = 2 are stable over weeks in frontal cortex. A, Collapse in the temporal profile of avalanches at Δt = 1 ms. Best collapse per recording day (*color bar*) for K-PF1 (*left*) and N-PM (*middle*). Rightmost column summarizes the normalized collapse motif (*norm.*) averaged across days for each NHP and cortical area. Shaded region indicates mean ± standard error per array within line thickness. **B,** The scaling exponent χ at which the best temporal profile collapse is obtained remains close to the theoretical value of 2 predicted for a critical branching process for all recording sessions. **C, D** Same as in *A*, *B* but at Δt = 30 ms demonstrating the characteristic parabolic profile for coarse-grained temporal scale. **E**, Same as in *A – D*, but nLFP events have been shuffled in time to remove spatial and temporal correlations. Note that the characteristic profile no longer traces a parabola as expected for critical dynamics. **F**, The scaling exponent χ is close to 1 when correlations are destroyed.

not change over time (Fig. 3B, D; for Δt = 1 ms, χ = 1.93 ± 0.14, linear regression fit of $1*10^{-2}$ ± 0.2; for Δt = 30 ms, χ = 2.01 ± 0.24, linear regression slope of $2*10^{-2}$ ± 0.04; Table 3 for individual arrays). In contrast, time-shuffled data reliably produced flattened motifs (Fig. 3E, F) with a scaling exponent close to 1, as found for non-critical dynamics, in which sizes grow linearly with duration (Villegas et al., 2019).

Persistence of integrative global network properties

In order to quantify in more detail the spatiotemporal correlations underlying persistent avalanche activity, we reconstructed functional networks from neuronal avalanches using the NC reconstruction (Pajevic and Plenz, 2009). This method uses a shortcut to Bayesian estimation of network connections, making it approximate, but also computationally efficient, and hence applicable to reconstructing relatively large networks from lengthy event train recordings (Fig. 4A). It also reduces the influence of indirect common input correlations and has been found in simulations to accurately and efficiently reconstruct the directed networks and weights from simulated point-process dynamics (Pajevic and Plenz, 2009). An example of the directed connectivity matrix for a single recording session derived from spontaneous avalanche activity is shown in Figure 4B. We found that for all arrays and recording sessions, the weights of the directed functional connections were not particularly heavy-tailed and distributed between an exponential and lognormal function over more than 3 orders of magnitude (Fig. 4C – E).

Having reconstructed the directed, weighted links in our avalanche-derived functional networks, we proceeded to calculate several graph theoretical properties. Integrative networks are characterized by a positive correlation, $R_{CL,}$ between the link cluster coefficient, C_L, and the corresponding link weight, w, between two nodes (Fig. 5A; (Pajevic and Plenz, 2012)). This

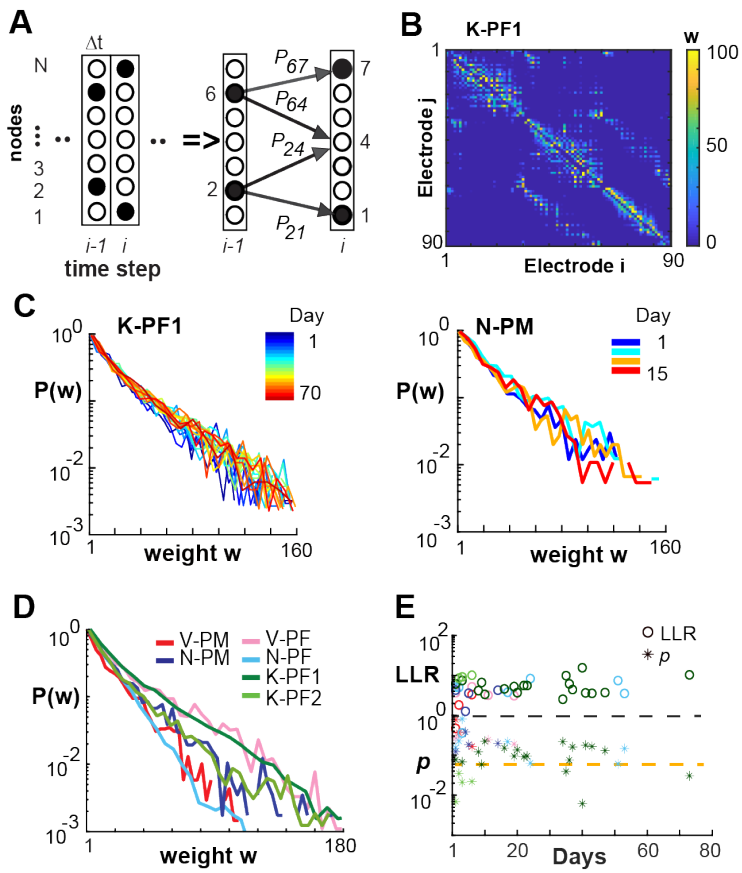

Figure 4: NC reconstruction of directed functional connectivity from ongoing LFPs reveals stable exponential distributions in link weights across time for all NHPs. A, Sketch of the NC algorithm. Active nodes (*filled circles*) at time Δt_{i-1} are evaluated regarding all existing prior probabilities (*solid* arrows) to obtain the pattern of active and inactive nodes at the next time step Δt_i (for details see (Pajevic and Plenz, 2009)). **B**, NC reconstructed network based on 15 minutes of nLFP activity at $\Delta t = 1$ ms from K-PF1 produces an adjacency matrix of weights w_{ij} showing sparse and mostly local functional connectivity. **C,** Normalized distributions in directed link strength for all recording days (*left*, K-PF1; *right*, N-PM). *Color bar*: recording day. **D,** Normalized probability distribution trends were consistent across areas and NHPs. Average distribution over all recording days. *Color code*: NHP-area. **E**, LLR (*open circles*) and *p* values (*asterisks*) for exponential vs. log-normal comparison of daily weight distributions (e.g. *C*) for all arrays and days (color code as in *D*).

positive correlation demonstrates that strongly connected nodes have more common neighbors compared to weakly connected nodes (Fig. 5B). We employed degree-sequence preserved randomization to subtract potential contributions to link clustering from the node degree distribution and report here the resulting excess link clustering, ΔC_L (see Material and Methods). The monotonic increase in ΔC_L with lowest-to-highest weight rank (Fig. 5C) clearly identifies integrative functional network organization in both PM and PF that was stable over time (Fig. 5D; linear regression slope of $5 \pm 10 \times 10^{-3}$; 95% confidence limit; see Table 4 for individual arrays).

Pruning analysis is an efficient approach to study the weight organization of networks (Onnela et al., 2007; Pajevic and Plenz, 2009). We found that pruning from the bottom, i.e. pruning weakest links progressively, had negligible effect on the network clustering properties. This was evidenced by a near constant value of the excess node clustering, ΔC, until the vast majority (80 – 90%, Fig. 5E; solid lines) of links were removed. In contrast, pruning from the top, i.e. removing the strongest links first, rapidly decreased ΔC, a result consistently found for all NHPs (Fig. 5E). We conclude that the integrative property arises from a "backbone" of strong links that is robust to weak-link pruning, yet quickly degrades when strong links are removed.

Entropy of mixing identifies link progression over many weeks

Given the stability observed over weeks in the global network dynamics, i.e., $\langle R \rangle$, α, χ, and integrative network organization, i.e., R_{CL}, we next sought to analyze in more detail the stability at the local level of individual link weights. Specifically, we examined whether the stability identified at the global level simply arises from stability at the local level. To quantify changes at the local level, we categorize the links, e.g., weak, medium, and strong, and analyze whether

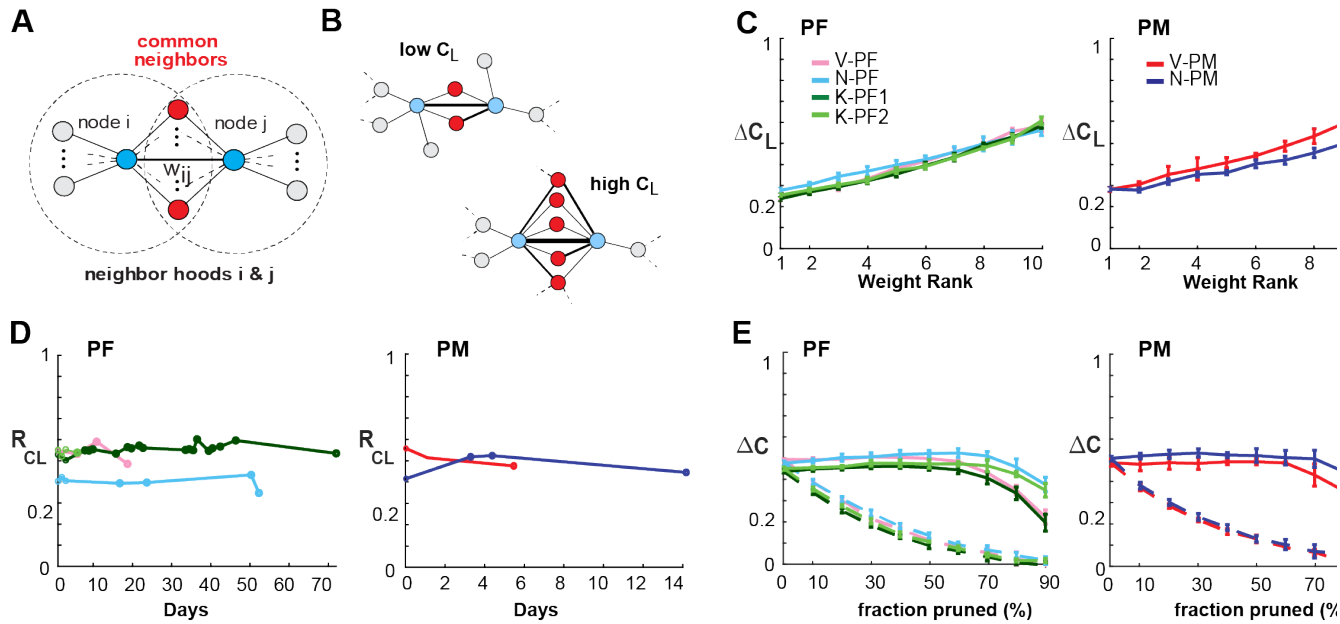

Figure 5: Link-clustering analysis reveals that integrative global network properties are stable over time. A, Schematic clustering diagram depicting two nodes (*blue*) connected by a link with weight w_{ij}. In an integrative network, the proportion of common neighbors (*red*) is expected to positively correlate with w_{ij}. **B,** Sketch of two subnetworks with low and high link clustering C_L respectively. **C,** The excess link clustering ΔC_L (see Methods) increases with link strength in all prefrontal (*left*) and premotor (*right*) cortical arrays (*color coded*; NHP-area). **D,** Analysis of cortical networks showed strongly positive R_{CL} over all recording sessions for up to 73 days. **E,** Link-pruning analysis of excess node clustering ΔC calculated via degree-sequence preserved randomization (Pajevic and Plenz, 2012) showed that the integrative clustering motif was robust to weak-link pruning (*solid lines*; error bars denote mean ± SD over all recordings for an array), while the clustering "backbone" of the network quickly degraded when strong links were pruned first (*dotted lines*; *color code* as in *D*). *C – E*, Δt = 1 ms.

178

links switch between categories over time, e.g., from weak to medium or vice versa. As a measure of mixing, we calculate the entropy of mixing, H_M, (see Methods). Two main factors contribute to potential changes in H_M, which originate from changes in link categories in a network from one day to another. First, independent random changes on each day will result in increased mixing and H_M, but not progressively over time. For example, errors in network reconstruction alone will result in a constant H_M over many days if the underlying network is not changing. Second, link weights could gradually evolve over days and weeks, and potentially change their categories, which is now progressively mixed and therefore is expected to lead to a monotonic increase in H_M until the maximum in mixing is reached. Because reconstruction errors are higher for weak links compared to strong links, we quantified potential changes in link weight from NC reconstructed networks separately for the strongest (top 50%) and weakest (bottom 50%) links. This separation is also motivated by our results for top- vs. bottom-pruning, which demonstrated that networks are less robust to link changes in the top half of the link weight distribution. For each half, we partitioned link weights further into strength quintiles, yielding 5 categories, and then studied whether members from different categories will mix over time. In figure 6, we show the data for the top half and bottom half and compare those curves to H_M obtained if the category labels were fully randomized at each step and also present the theoretical maximum for H_M (see also Material and Methods). Because all successive distributions used the link labels derived from Day 1 (making $H_M = 0$), the average entropy of mixing was plotted beginning from the second recording for each NHP. For all arrays, we found that H_M for the bottom half of links reaches close to the maximal entropy by the following day demonstrating that weak links fluctuate randomly. On the other hand, we found

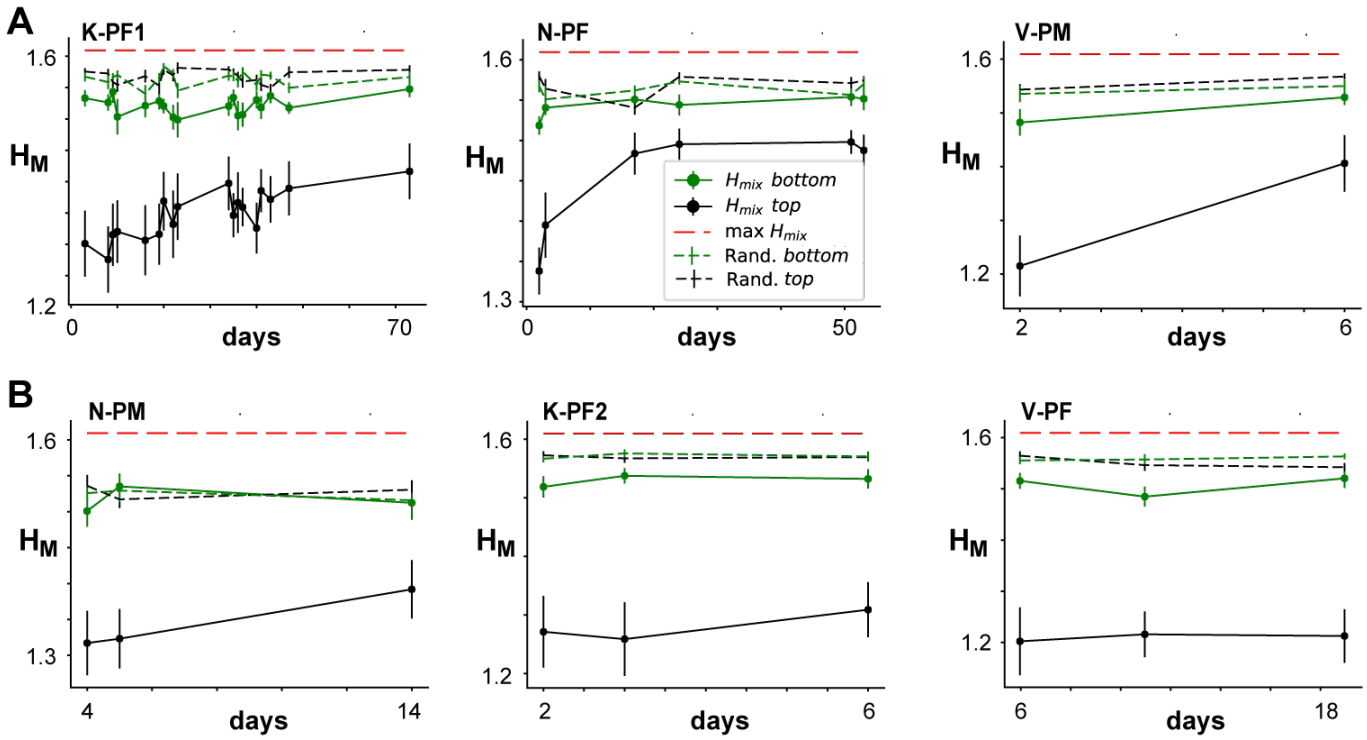

Figure 6: Entropy of mixing analysis demonstrates progressive changes in strong links over time for some networks. Entropy of mixing (H_M) analysis of the link weights obtained with NC reconstructions from Δt = 1 ms raster recordings. H_M is plotted for the "top" half (strongest 50% of links; *black curves*) and "bottom" half (weakest 50% of links; *green curves*) versus the days after the initial recording. The black and green dashed lines indicate corresponding H_M obtained when the labels were fully randomized, while the red dashed line indicates the theoretical maximum of H_M. The six panels represent six different arrays from the three monkeys shown in two rows. **A**, Arrays for which statistically significant progression of mixing was obtained for "top" links. **B**, Arrays for which no statistically significant progression was observed. The "top" half of the links consistently showed lower H_M than the "bottom" half of the links, which is mainly due to the smaller reconstruction error. The Day 1 points are not plotted because, by default of our labeling, the initial value for H_M is zero.

201

progressive and statistically significant increases of H_M over subsequent days for strong links in three out of six arrays (Figure 6A, B; see Table 4). These findings demonstrate stability in avalanche dynamics and integrative network organization even though the network undergoes significant weight reorganization at the individual link level.

Discussion

Fluctuations in ongoing neuronal activity give rise to functional networks that allow for the categorization of healthy and pathological brain states (Bullmore and Sporns, 2009; Fox and Raichle, 2007; Raichle, 2015), yet, the dynamical and graph theoretical markers underlying these ongoing fluctuations have been challenging to identify. By recording the LFP in prefrontal and premotor cortex of NHPs over weeks at high spatiotemporal resolution, we established two robust markers of ongoing activity; the dynamical category of neuronal avalanches and the graph theoretical category of integrative networks. Avalanche dynamics revealed power law statistics, parabolic temporal profiles and a scaling exponent of 2 in support of critical branching process dynamics (di Santo et al., 2017; Miller et al., 2019; Sethna et al., 2001). We further demonstrate that avalanches form integrative networks despite reorganization of individual link weights as identified using NC estimators and an entropy of mixing approach (Onnela et al., 2007; Pajevic and Plenz, 2009, 2012). Our results suggest that avalanche dynamics and corresponding integrative networks identify a robust state of the awake frontal cortex. This work should be impactful for computational studies of cortex function and for translational research into the identification of brain dynamics in healthy subjects and corresponding deviation in brain disorders.

Recent analysis of evoked cortical activity in nonhuman primates during behavior demonstrated the preservation of neuronal avalanche dynamics in the face of transient activity changes, specifically the nLFP rate (Yu et al., 2017). Given the robustness of integrative network properties observed in combination with avalanche dynamics *in vitro* (Pajevic and Plenz, 2009, 2012) as well as *in vivo* (the present study), we would expect integrative networks properties to also persist during behavioral tasks.

Stability of LFP based avalanches and relation to neuronal activity

Technical advances in identifying long-term robustness in neuronal activity using cellular resolution approaches (Dickey et al., 2009; Fraser and Schwartz, 2011; Jackson and Fetz, 2007; Li et al., 2017; Nicolelis et al., 2003; Tolias et al., 2007) typically suffer from spatial and temporal subsampling (Levina and Priesemann, 2017; Petermann et al., 2009; Ribeiro et al., 2010; Ribeiro et al., 2014) limiting proper identification of avalanche dynamics and corresponding reconstruction of functional connectivity. The LFP, on the other hand, is a robust neuronal population signal, less prone to spatial subsampling and at high temporal resolution contains local spike information particularly when recorded from superficial layers (Donoghue et al., 1998; Mehring et al., 2003; Petermann et al., 2009; Rasch et al., 2008). Indeed, we recently demonstrated in nonhuman primates and *in vitro* slices that single neurons selectively participate in expansive, repeated LFP avalanches (Bellay et al., 2021), which suggest that the stability observed in the present study for LFP-based avalanches might extend to the single neuron level.

Experimental manipulations support a homeostatic regulation of avalanche dynamics in cortex. Transient pharmacological perturbation *in vitro* (Plenz, 2012) or sensory deprivation *in vivo* (Ma et al., 2019) initially abolishes avalanche dynamics, which is followed by a recovery

over several days. Developmental findings further support an autonomous regulation of neuronal avalanches in isolated cortex *in vitro* in the absence of sensory input (Pasquale et al., 2008; Stewart and Plenz, 2007; Tetzlaff et al., 2010). Identifying the homeostatic regulation of avalanche dynamics and integrative networks will require precise perturbation approaches (Chialvo et al., 2020) in combination with advanced cellular techniques suitable for long-term monitoring such as ratiometric genetically-encoded calcium indicators (GECIs), which naturally compensate for cell-intrinsic expression variability (Lutcke et al., 2013).

NC reconstruction of integrative networks

Reconstruction of our directed, weighted functional networks utilized a Bayesian-derived NC approach, which is easily scalable to large networks (Pajevic and Plenz, 2009, 2012) and reduces correlations from common input. Network simulations demonstrated ground-truth reconstruction for various small-world topologies from subcritical, supercritical and critical dynamics, the latter in line with reconstructions from observed avalanche activity (Pajevic and Plenz, 2009).

Here we used significant events in LFP fluctuations, i.e. nLFPs, for the reconstruction of functional connectivity, which differs from the more common ansatz based on continuous timeseries. Accordingly, our approach, which selectively reconstructs synchronization dynamics in the form of avalanches, introduces a time scale Δt to which the NC reconstruction is sensitive. In order to identify the spatiotemporal spread of avalanches, the use of a microelectrode array introduces a spatial discretization, which consequently enforces a discretization Δt in time. It was found empirically that Δt should be linked to the average propagation velocity of neuronal activity in the network, allowing Δt to be approximated by $\langle IEI \rangle$ (Beggs and Plenz, 2003; Petermann et al., 2009). For Δt smaller than $\langle IEI \rangle$, errors of prematurely terminating avalanches

increase, whereas errors of concatenating successive avalanches increase for Δt larger than <IEI>. An approximate balance regarding these two errors is struck for Δt = IEI. With respect to NC reconstruction, increasing Δt will increase the count in nLFP occurrences on the array per time step, resulting in an increase in the computational load and increased error in estimating priors for potentially activated links. Accordingly, we chose a Δt slightly smaller than IEI for a conservative and balanced estimate of the functional connectivity based on avalanche propagation.

Integrative networks differ from networks in which the weight is positively correlated with the node degree (Barrat et al., 2004; Bianconi, 2005; Pajevic and Plenz, 2012). Our shuffling correction further demonstrates that the organization of weighted links in integrative networks cannot be simply explained by the link-degree distribution and in which strong links are part of a continuous, in our case near exponential distribution (*cf*. Fig. 4D). Integrated networks are also not a simple consequence of critical branching processes generating avalanches, which can be realized in many topologies and architectures (Pajevic and Plenz, 2009, 2012).

Robust avalanche scaling of $\chi = 2$ over many weeks

Heterogeneous activity in the form of neuronal avalanches has been the hallmark of ongoing (Beggs and Plenz, 2003; Bellay et al., 2015) and evoked (Yu et al., 2017) brain activity in superficial layers of the cerebral cortex. The scale-invariant hallmark of avalanches has been found to capture ongoing neuronal activity in nonhuman primates at the mesoscopic level in the LFP (Klaus et al., 2011; Petermann et al., 2009; Yu et al., 2014; Yu et al., 2017; Yu et al., 2011) and macroscopic activity measured with EEG (Meisel et al., 2013), MEG (Shriki et al., 2013)

289 and fMRI (Fraiman and Chialvo, 2012; Tagliazucchi et al., 2012). The observed power law
290 distributions in cluster size and duration support the idea that the cortex operates close to a
291 critical state at which networks gain numerous advantages in information processing (Beggs and
292 Plenz, 2003; Gautam et al., 2015; Kinouchi and Copelli, 2006; Shew et al., 2009; Shew et al.,
293 2011; Yang et al., 2012).

294 Our present demonstration of an inverted-parabolic avalanche shape, collapse exponent
295 of 2 and size distribution slope >-2 is in line with predictions that the unfolding of avalanches in
296 the adult brain is governed by a critical branching process (for details see (Miller et al., 2019)).
297 This profile demonstrates that the initial spatial unfolding of an avalanche in time is truly
298 expansive and should not be viewed as being dominated by a few strong links. Recently,
299 avalanches with a scaling factor of 2 have been described for whole-brain neuronal activity in the
300 zebrafish larvae (Ponce-Alvarez et al., 2018), however, the corresponding size and duration
301 exponent were significantly steeper compared to reports for the mammalian cortex, suggesting a
302 different dynamical model for the zebrafish.

303 Connectome analyses on a time scale of seconds have identified transient fluctuations in
304 functional connectivity reflecting distinct states (Hutchison et al., 2013; Liu and Duyn, 2013;
305 Zalesky et al., 2014), which based on computational modeling were found to be intermittent, a
306 signature of metastability (Deco et al., 2017; Hansen et al., 2015). Because our analysis was
307 based on nLFPs and not continuous time signals, we were unable to obtain NC reconstructed
308 networks for shorter time periods than 15 – 30 min. In fact, our entropy of mixing analysis
309 allowed for an assessment of link weight progression in the face of reconstruction errors due to
310 limited data availability. Transient fluctuations in functional connectivity estimates are not in

contrast to the reorganization of links reported in our study. Short-term fluctuations in the face of long-term stability are hallmarks of critical dynamics (Fraiman and Chialvo, 2012; Tagliazucchi et al., 2012).

Potential advantages of avalanche dynamics and integrative networks for cortex function

Anatomically, the mammalian cortex is a sheet of local, functional modules that dynamically combine to support complex brain functions (Braitenberg and Schüz, 1991; Honey et al., 2007). Local connectivity ensures diverse local operations whereas long-range connections support global coordination (e.g. (Bullmore and Sporns, 2009; Kirst et al., 2016)). These structural hallmarks are dynamically realized in neuronal avalanches, which support a scale-free and selective organization of neuronal synchronization over all distances. They are graph theoretically embedded in integrative networks, which maintain a high level of node clustering until about 90% of the strongest links are pruned, i.e. about 10% of strong links are used for long-range connections. Intriguingly, simulations identified a particular local learning rule that operates on activity cascades such as avalanches to build integrative networks from random networks (Pajevic and Plenz, 2012). The rule increases link weights at locations of recent cascade failure, thereby facilitating the unfolding of future avalanches (Alstott et al., 2015). This mechanism opens bottlenecks in the network and further supports activity propagation over long distances. We therefore hypothesize that avalanche dynamics in combination with integrative network organization are beneficial for local operational diversity while supporting long-range, selective propagation of information.

Material and Methods

Animal procedures

All animal procedures were conducted in accordance with NIH guidelines and were approved by the Animal Care and User Committee of the National Institute of Mental Health. Three adult NHPs (*Macaca mulatta*; 1 male, 2 females; 7–8 years old) received two chronic implantations of high-density 96-microelectrode arrays each (Blackrock Microsystems; 4×4 mm^2; 400 µm interelectrode distance; 10×10 grid with corner grounds). To direct recordings towards superficial cortical layers II/III, electrode shanks of 0.6 mm length were used in prefrontal cortex (PF; n = 4), and shanks of 1 mm length were used for premotor cortex (PM; n = 2). During recording sessions monkeys sat head-fixed and alert in a monkey chair with no behavioral task given. Portions of this dataset have been analyzed previously (Bellay et al., 2021; Meisel et al., 2013; Miller et al., 2019; Yang et al., 2012; Yu et al., 2014).

Local field potential recordings in awake monkeys

Simultaneous and continuous extracellular recordings were obtained for 12 – 60 min per recording session (2 kHz sampling frequency), band-pass filtered between 1 – 100 Hz (6th-order Butterworth filter) to obtain the local field potential (LFP), and notch-filtered (60 Hz) to remove line noise. About 2 ± 1% of time periods were removed from functional electrodes due to artifacts introduced by e.g. vocalization, chewing, sudden movements. These artifacts were identified by threshold crossing (SD > 7) and excised (± 0.25 s). Arrays on average contained 86 ± 8 functional electrodes that exhibited 64 ± 50 µV of spontaneous LFP fluctuations (SD). Channels which had been removed from an array at any recording day were discounted for all recording days. Electrode LFPs were z-transformed and recording sessions for each array were

analyzed individually. The current study represents a combined 26 hr of ongoing cortical LFP activity.

Neuronal avalanche definition and temporal resolution

For each electrode in the array, peak amplitude and time of negative LFP (nLFP) threshold crossings (–2 SD) were extracted at the temporal resolution of Δt = 0.5 ms given our sampling rate of 2 kHz. We note that the negative peak amplitude of the LFP correlates with the probability of extracellular unit firing and synchrony in nonhuman primates (Bellay et al., 2021; Petermann et al., 2009). The mean inter-event interval, <IEI>, defined as the average time between consecutive nLFPs among all functional electrodes on the array, was calculated. We then binned nLFP times in steps of Δt = <IEI> for each electrode, which ranged between 3 – 4 ms across NHPs and arrays. All nLFP events from all electrodes were combined into a matrix, i.e. raster, with rows representing electrodes and columns representing time steps. A population time vector was obtained by summing nLFPs in the raster for each time step. Avalanches were defined as spatiotemporal continuous activity in the population vector bracketed on each side by at least one time bin of duration Δt with no nLFP. The size of an avalanche, S, was defined as the number of nLFPs participating. Multiple nLFPs at an electrode during an avalanche are rare (Yu et al., 2014) and were counted in size estimates. Scale-invariance of S was visualized by plotting probability distributions P(S) in double-log coordinates. We previously showed that analyzing nLFP at Δt = <IEI> results in a distribution of avalanches with a slope close to -3/2 in line with expectations for a critical branching process (e.g., (Beggs and Plenz, 2003)).

The maximum log-likelihood ratio (LLR) was calculated to test potential power law distributions in avalanche size S against the alternatives of exponential or log-normal distribution

models (Clauset et al., 2009; Klaus et al., 2011). When tested positive for power law, the LLR estimate for best slope α was reported. Here we used the range of $S = 1$ to 40, which excludes the distribution cut-off (Klaus et al., 2011) close to the total number of functional electrodes on the array (n >70). We note that analyzing avalanche dynamics at different temporal resolutions, e.g. at shorter Δt or longer Δt compared to the <IEI>, increases or decreases the slope α respectively, but not the power law form itself (see also Table 1; (Beggs and Plenz, 2003, Petermann, 2009 #4926)).

Avalanche temporal profile collapse and scaling exponent

Given the difficulty of obtaining robust lifetime distributions in the presence of ongoing oscillations, the stability analysis for avalanches in the present work focused mainly on the calculation of size distributions and temporal profile collapse (for details see Miller, 2019 #45}. The temporal profile, $S(t)$, was described by the number of participating electrodes at each timestep t = 1 up to the avalanche lifetime, L, which was defined by the number of timesteps Δt that the avalanche persisted. In line with our previous results, profile analysis was carried out at $\Delta t = 1$ ms and $\Delta t = 30$ ms to avoid profile modulation by ongoing γ-oscillations (Miller et al., 2019). Avalanches were grouped by L in multiples of Δt and averaged to obtain the mean temporal profile for a given lifetime, $\langle S\rangle(t, L)$. After normalizing to dimensionless time units, i.e., the relative lifetime, t/L, amplitudes were then rescaled via Equation 1.

$$\langle \mathrm{S}\rangle\left(\frac{t}{L}\right) \sim \mathrm{L}^{\chi-1}\ \boldsymbol{\mathcal{F}}\left(\frac{t}{L}\right) \tag{1}$$

The profile collapse function, shown in Equation 1, relates the mean profile for each lifetime L, $\langle S\rangle(t/L)$, with a characteristic temporal motif $\boldsymbol{\mathcal{F}}(t/L)$, and scaling factor, $L^{\chi-1}$, which is independent of L according to Equation 1. To perform a shape collapse, we plotted $\langle S\rangle(t, L)$ from

L-1 through L+1 for $L_{\min} = 4\Delta t$ (to reduce finite size effects in shape caused by too few data points). The collapse error, Δ_F, was quantified via a normalized mean-squared error (NMSE) of height-normalized individual profiles to the combined normalized average of all collapsed profiles, $\boldsymbol{\mathcal{F}}(t/L)$. Minimized collapse error was calculated by scanning through $\chi = 0.5$ to 3 at resolution of 0.001 to find the collapse in avalanche waveform associated with the smallest Δ_F via χ_{collapse}. A value of $\Delta_F > 1$ was considered a failure in collapse.

We note that for fractal objects such as spatiotemporal avalanches, changing the temporal resolution also partitions avalanches differently. For a $\Delta t = 1$ ms, avalanche durations in multiples of Δt will exhibit a power law as well as for $\Delta t = 30$ ms (see e.g. (Miller et al., 2019)). Accordingly, the temporal profile of avalanches must be examined in multiples of generations of duration Δt. A comparison between timescales in absolute times may not be possible. In the present study, an avalanche of duration 150 ms encompasses L = 5 generations at $\Delta t = 30$ but would require L = 150 generations at $\Delta t = 1$, which is highly unlikely to occur.

Fit of the average temporal profile of avalanches

For the parabolic fit we used the approach by (Laurson et al., 2013) as follows:

$$\mathrm{y} = \mathrm{A} \cdot \frac{t}{T}\left(1 - \frac{t}{T}\right)^{\gamma - 0.5} \tag{2}$$

The parabolic fit error, Δ_{parab}, was quantified via a normalized mean squared error (NMSE) of individual profiles to an amplitude-matched parabola which was coarse-grained to match L. Comparison to a semicircle fit was conducted in the same manner to obtain Δ_{semi} using

$$\mathrm{y} = \mathrm{A} \cdot \sqrt{1 - \left({}^{t}/_{T}\right)^{2}}\,. \tag{3}$$

Correlation-based network reconstruction

Networks were reconstructed for each recording session individually and the links with low pairwise correlations were removed before subsequent network analysis. Rather than applying a strict minimum correlation threshold for removing the links, which would leave our analysis vulnerable to inter-NHP differences in electrode impedances, etc., we instead sequentially removed the weakest links in 0.01 increments of the correlation threshold until a predefined sparsity of approximately 40% was achieved. Weight bins were divided into deciles for pruning analysis (Fig. 4).

Normalized Count reconstruction of network

To remove the influence of common input to electrodes on the array, which inflates the Pearson's pairwise correlation, we conducted a network reconstruction. This nonparametric method, called the NC approach, is used for the network reconstruction because its computational efficiency is comparable to the correlation analysis yet with much lower reconstruction error, which are important considerations for analysis of long LFP time series collected in awake *in vivo* preparations. For this reconstruction, the time-window within which active nodes can influence each other was examined for 0.5, 1, <IEI>, and 30 ms. For each node activation (spike), all nodes that were active within Δt, prior to the spike, were deemed as potential causes. Results were very similar for Δt = 0.5 and 1 ms (data not shown). For longer Δt, the precision of the algorithm decreases rapidly due to (1) the increase in ambiguous potential associations between the number of active nodes in successive frames and (2) a decrease in the number of transition time steps to estimate link weights (Pajevic and Plenz, 2009). Here we show results for Δt = 1 ms, which matches our avalanche scaling analysis.

Integrative networks and Pruning analysis

Once the networks were defined, we studied their integrative properties (Pajevic and Plenz, 2012). The link clustering coefficient, C_L, was defined for each link as the ratio of the number of common neighbors of its end nodes to the number of all neighbors (see Fig. 4A). In an integrative network, there is a positive correlation R_{CL} between C_L and the weight of the link, indicating that strongly connected nodes are likely to share more common neighbors. To visualize this correlation, we divide links based on their weight into equally sized 10 blocks ranging from the weakest block (rank 1) to the highest rank. For each block, we obtain the average C_L and subtract the equivalent value that is obtained from the degree preserved randomized network, yielding the excess link clustering, ΔC_L. We also conducted a "pruning analysis" in which we studied the robustness of the excess node clustering ΔC upon the progressive removal of the weakest (bottom pruning) or strongest (top pruning) links. Similarly, the excess node clustering, ΔC, was defined as the difference of the mean clustering coefficient of the original network and the corresponding randomized network after the degree-sequence preserved randomization.

Entropy of mixing analysis

The estimated link weights fluctuated over time in both pairwise correlation and in directed networks obtained with the NC reconstruction algorithm. We sought to explore whether these fluctuations predominantly represent an error in the network reconstruction or arise from a genuine and progressive change in the underlying network weights. To answer this question, we developed a novel method that utilizes the entropy of mixing to quantify the progression of these fluctuations in individual link strengths from one day to another. The entropy of mixing is a concept from thermodynamics and describes the increase in total entropy when partitioned (pure

and equilibrated) sub-systems are allowed to mix. It is quantified using the Shannon entropy in which probabilities are replaced by the fractions of each of the original species found at different partitions. Hence, to conduct our entropy of mixing analysis, we need to partition the links into different categories. Labels are assigned according to the magnitude of their weights obtained from the Day 1 data, and partitioning them into a finite set of categories, N_c, ranging from the weakest links to the strongest links. In our case, we used $N_c = 5$, so that the label $c = 1$ marked the weakest 20% of the sorted links and incrementally, c = 5 marked the strongest 20% of the links.

We conducted the mixing analysis on two different and complementary sub-networks. The first is the "top" network, consisting of the 50% of the strongest links, and the second is the "bottom" network, consisting of the weakest 50% percent of links. This was done mainly to have some test of the performance of the entropy of mixing analysis, as we expect that the "bottom" half is more dominated by the reconstruction errors of the NC algorithm than the "top" half. Note that with this two-stage stratification of the links, the strongest 20% links in the "top" network are effectively representing the 10% of strongest links in the full network, while the weakest 20% of the "top" network links have still greater magnitude than the strongest quintile of the "bottom" networks, and, *vice versa*, the weakest 20% of the links in the "bottom" represent the 10% of weakest links in the full network. Once the chosen links were labelled, we then monitored the changes of their weights over subsequent days. Specifically, we sort them again based on their new weights, but now partition them over a potentially larger number of weight groups, $N_g = k\, N_c$, where k is an integer, in order to make all groups contain a single category label for the Day 1 stratification (we use k = 3 and $N_g = 15$, meaning that the links in the groups 1 through 3 will all initially carry the label c = 1, the groups g = 4 – 6 will be labeled c = 2, etc).

Due to (1) reconstruction errors and (2) potential actual network weight changes from one day to another, each of the groups will on the subsequent days contain a mixture of the original labels, although it is expected that the low group indices, g, will early on predominantly carry the labels of the weak links, and *vice versa*. For each group, we calculate a fraction, f_c, of the links that carry label c, which by definition are normalized to 1, i.e., $\sum_{c=1}^{N_c} f_c = 1$. For each group g we then calculate the Shannon entropy of such mixture according to $H_g = -\sum_{c=1}^{N_c} f_c \log f_c$. Finally, we report the average and the standard error over all non-edge H_g values, i.e., excluding the extreme groups, g = 1 and g = 15, as those have only uni-directional mixing (n = N_g-*2 = 13*). Hence, the average entropy of mixing reported in our results is $H_M = \frac{1}{N_g-2}\sum_{g=2}^{N_g-1} H_g$.

To evaluate if we have seen a progression in the weight evolution, we test it against the null hypothesis that there was no significant linear trend across the subsequent days. To do so we use a Monte Carlo (MC) procedure, in which we generate one million normally-distributed replicates, N(0,σ_G) for each point, where σ_G are the standard deviations of the means obtained using the non-edge groups described in the previous paragraph. For each of the N_{MC} = 1000000 replicates we perform a linear regression and count the number of times the MC slopes were greater than the slope we obtained using the mean values for H_M. From this count, N_{pos}, our estimate of the p values is $p = (N_{\text{pos}}+1)/(N_{MC}+1)$ (see Table 4).

Tables

Table 1. Summary of average estimates for the mean Pearson's pairwise correlation coefficient, <*R*>, the exponent α of avalanche size distributions for each nonhuman primate and array at temporal resolutions of Δt = 1 ms and Δt = 30 ms respectively. Exponents were derived from maximum likelihood estimates. Stability of α over all recording days was quantified by the linear regression slope within 95% confidence limits (CfL).

	<R> Stability	**Avalanche size distribution (Δt = 1 ms)**	**slope α stability (Δt = 1 ms)**	**Avalanche size distribution (Δt = <IEI>)**	**slope α stability (Δt = <IEI>)**	**Avalanche size distribution (Δt = 30 ms)**	**slope α stability (Δt = 30 ms)**
	Regression slope (95% CfL) ($\times 10^{-3}$)	Exponent α (± SD)	Regression slope (95% CfL) ($\times 10^{-3}$)	Exponent α (± SD)	Regression slope (95% CfL) ($\times 10^{-3}$)	Exponent α (± SD)	Regression slope (95% CfL) ($\times 10^{-3}$)
V-PF	-1 (-3, 2)	1.71 ± 0.00	0 (-1, 0)	1.26 ± 0.01	-2 (-3, 3)	0.65 ± 0.03	-3 (-9, 2)
V-PM	0 (-62, 62)	1.64 ± 0.02	6 (-40, 51)	1.29 ± 0.04	16 (-28, 60)	1.12 ± 0.05	20 (-2, 43)
N-PF	1 (0, 2)	1.71 ± 0.02	-1 (-1, 0)	1.41 ± 0.01	0 (-1, 0)	0.97 ± 0.02	0 (-1, 1)
N-PM	1 (-13, 15)	1.73 ± 0.02	2 (-8, 12)	1.31 ± 0.02	0 (-1, 1)	0.75 ± 0.02	3 (-6, 12)
K-PF1	1 (0, 1)	1.65 ± 0.02	-1 (-1, 0)	1.29 ± 0.01	0 (-1, 0)	0.90 ± 0.02	0 (0, 1)
K-PF2	0 (-20, 20)	1.77 ± 0.03	5 (-33, 43)	1.36 ± 0.02	1 (-27, 29)	0.74 ± 0.03	10 (-16, 35)
Mean ± SD	**0 ± 1**	**1.70 ± 0.05**	**2 ± 3**	**1.32 ± 0.05**	**3 ± 7**	**0.86 ± 0.17**	**5 ± 9**

Table 2. Summary of scaling function estimate for the temporal profile of neuronal avalanches. A parabolic fit (Δ_{parab}) is compared to a semicircle fit (Δ_{semi}) at temporal resolutions Δt = 1 ms and Δt = 30 ms for each nonhuman primate and array and its corresponding phase-randomized profile (*random*) at Δt = 1 ms.

	Temporal Profile Fit: Parabola vs. Semicircle RMSE (Δt = 1 ms)		**Temporal Profile Fit: Parabola vs. Semicircle RMSE (Δt = 30 ms)**		**Random Profile Fit: Parabola vs. Semicircle RMSE (Δt = 1 ms)**	
	Paired t-Test (*p*-value)	ANOVA (F)	Paired t-Test (*p*-value)	ANOVA (F)	Paired t-Test (*p*-value)	ANOVA (F)
V-PF	4.36E-05	110.44	2.00E-04	62.26	5.96E-10	4832.54
V-PM	3.87E-04	121.17	3.40E-05	417.07	7.82E-07	2776.65
N-PF	6.12E-11	460.49	2.66E-13	1156.15	3.74E-14	1607.96
N-PM	6.81E-08	991.66	3.15E-06	272.38	2.41E-10	6533.12
K-PF1	2.76E-22	472.2	2.41E-25	715.09	1.98E-50	18530.05
K-PF2	2.60E-06	290.68	9.64E-06	186.09	1.91E-09	3277.87
Fit Error Δ	$\Delta_{parab} < \Delta_{semi}$	$\Delta_{parab} < \Delta_{semi}$	$\Delta_{parab} < \Delta_{semi}$	$\Delta_{parab} < \Delta_{semi}$	$\Delta_{parab} > \Delta_{semi}$	$\Delta_{parab} > \Delta_{semi}$

515 **Table 3.** Summary of estimates for the scaling exponent χ to optimally collapse temporal
516 avalanche profiles at temporal resolutions Δt = 1 ms and Δt = 30 ms for each nonhuman primate
517 and array. The stability of χ across all recording days was quantified by the linear regression
518 slope reported and 95% confidence limits. *Random*: Phase randomized control of temporal
519 avalanche profile.
520

	Scaling Exponent χ (*Δt* = 1 ms)	**χ Stability (*Δt* = 1 ms)**	**Scaling Exponent χ (*Δt* = 30 ms)**	**χ Stability (*Δt* = 30 ms)**	**Scaling Exponent χ Random (*Δt* = 1 ms)**	**χ Stability Random (*Δt* = 1 ms)**
	Mean χ (± SD)	Regression slope (95% CfL)	Mean χ (± SD)	Regression slope (95% CfL)	Mean χ (± SD)	Regression slope (95% CfL)
V-PF	1.78 ± 0.05	0.002 (-0.019, 0.022)	1.61 ± 0.09	-0.01 (-0.02, 0.01)	1.15 ± 0.01	0.001 (-0.001, 0.003)
V-PM	1.93 ± 0.15	0.051 (-0.3, 0.4)	2.25 ± 0.20	0.06 (-0.6, 0.7)	1.15 ± 0.00	0.000 (-0.001, 0.002)
N-PF	2.10 ± 0.06	0.002 (-0.000, 0.004)	2.15 ± 0.15	-0.00 (-0.01, 0.00)	1.14 ± 0.03	0.000 (-0.001, 0.002)
N-PM	2.05 ± 0.13	0.011 (-0.053, 0.075)	1.85 ± 0.05	0.005 (-0.016, 0.027)	1.14 ± 0.01	0.002 (-0.005, 0.008)
K-PF1	1.92 ± 0.03	0.000 (-0.001, 0.001)	2.11 ± 0.1	-0.000 (-0.003, 0.003)	1.15 ± 0.01	0.000 (-0.000, 0.000)
K-PF2	1.76 ± 0.02	0.007 (-0.004, 0.018)	2.12 ± 0.20	0.086 (-0.029, 0.2)	1.15 ± 0.00	0.000 (-0.004, 0.005)
Mean ± SD	**1.93 ± 0.14**	**0.012 ± 0.19**	**2.01 ± 0.24**	**0.02 ± 0.04**	**1.15 ± 0.01**	**0.001 ± 0.001**

521 **Table 4.** Functional network stability based on NC reconstruction algorithm at Δt = 1. Shown is
522 the stability of R_{CL} over time (see also Fig. 5D). H_M *p*-values given for top 50% and bottom 50%
523 for significant trend in mixing observed.

524

	R_{CL} **Stability** **(*Δt* = 1 ms)**	***H_M*** **Trend** **(*Δt* = 1 ms)**	
	Regression slope (95% CfL) ($\times 10^{-3}$)	Top 50% *p*	Bottom 50% *p*
V-PF	-1 (-28, 18)	0.46	0.34
V-PM	0 (-62, 62)	0.007	0.05
N-PF	1 (0, 0.002)	$<10^{-5}$	0.03
N-PM	14 (-13, 15)	0.08	0.54
K-PF1	1 (0, 1)	0.003	0.2
K-PF2	0 (-20, 21)	0.27	0.35
Mean ± SD	**5 ± 10**		

Acknowledgements

We thank members of the Plenz lab and attendees of the "*Critical brain dynamics: 5th International Workshop on Criticality and the Brain*", 2016, NIH, USA for their support and useful discussions.

Funding sources

This research was supported by the Intramural Research Program of the National Institute of Mental Health ZIAMH002797, USA to D.P. and the *Eunice Kennedy Shriver* National Institute of Child Health and Human Development to S.P. This research utilized the computational resources of the NIH HPC Biowulf cluster (http://hpc.nih.gov).

Author Contributions

S.Y. collected the data; S.R.M. , S.Y. and S.P. analyzed the data; S.R.M., S.Y., S.P. and D.P. wrote the manuscript.

Supplementary Information

No Supplementary Information.

Competing interests:

The authors declare no competing interests.

References

Alstott, J., Pajevic, S., Bullmore, E., and Plenz, D. (2015). Opening bottlenecks on weighted networks by local adaptation to cascade failures. Journal of Complex Networks *3*, 552-565.

Barrat, A., Barthelemy, M., Pastor-Satorras, R., and Vespignani, A. (2004). The architecture of complex weighted networks. Proc Natl Acad Sci U S A *101*, 3747-3752.

Bassett, D.S., and Sporns, O. (2017). Network neuroscience. Nat Neurosci *20*, 353-364.

Beggs, J.M., and Plenz, D. (2003). Neuronal avalanches in neocortical circuits. J Neurosci *23*, 11167-11177.

Bellay, T., Klaus, A., Seshadri, S., and Plenz, D. (2015). Irregular spiking of pyramidal neurons organizes as scale-invariant neuronal avalanches in the awake state. eLife *4*, e07224.

Bellay, T., Shew, W.L., Yu, S., Falco-Walter, J.J., and Plenz, D. (2021). Selective participation of single cortical neurons in neuronal avalanches. Frontiers in Neural Circuits *14*.

Bianconi, G. (2005). Emergence of weight-topology correlations in complex scale-free networks. EL *71*, 1029-1035.

Braitenberg, V., and Schüz, A. (1991). Anatomy of the Cortex: Statistics and Geometry (Berlin Heidelberg New York: Springer-Verlag).

Bullmore, E., and Sporns, O. (2009). Complex brain networks: graph theoretical analysis of structural and functional systems. Nat Rev Neurosci *10*, 186-198.

Chialvo, D.R., Cannas, S.A., Grigera, T.S., Martin, D.A., and Plenz, D. (2020). Controlling a complex system near its critical point via temporal correlations. Scientific Reports *10*, 12145.

Clauset, A., Shalizi, C.R., and Newman, M.E.J. (2009). Power-law distributions in empirical data. SIAM Rev *51*, 661 - 703.

Deco, G., Kringelbach, M.L., Jirsa, V.K., and Ritter, P. (2017). The dynamics of resting fluctuations in the brain: metastability and its dynamical cortical core. Scientific Reports *7*, 3095.

di Santo, S., Villegas, P., Burioni, R., and Muñoz, M.A. (2017). Simple unified view of branching process statistics: Random walks in balanced logarithmic potentials. Phys Rev E *95*, 032115.

569 Dickey, A.S., Suminski, A., Amit, Y., and Hatsopoulos, N.G. (2009). Single-unit stability using
570 chronically implanted multielectrode arrays. J Neurophysiol *102*, 1331-1339.

571 Donoghue, J.P., Sanes, J.N., Hatsopoulos, N.G., and Gaál, G.n. (1998). Neural discharge and
572 local field potential oscillations in primate motor cortex during voluntary movements. J
573 Neurophysiol *79*, 159-173.

574 Fox, M.D., and Raichle, M.E. (2007). Spontaneous fluctuations in brain activity observed with
575 functional magnetic resonance imaging. Nat Rev Neurosci *8*, 700-711.

576 Fraiman, D., and Chialvo, D.R. (2012). What kind of noise is brain noise: anomalous scaling
577 behavior of the resting brain activity fluctuations. Front Physiol *3*, 307.

578 Fraser, G.W., and Schwartz, A.B. (2011). Recording from the same neurons chronically in motor
579 cortex. J Neurophysiol *107*, 1970-1978.

580 Gautam, H., Hoang, T.T., McClanahan, K., Grady, S.K., and Shew, W.L. (2015). Maximizing
581 sensory dynamic range by tuning the cortical state to criticality. PLoS Comput Biol *11*,
582 e1004576.

583 Hansen, E.C.A., Battaglia, D., Spiegler, A., Deco, G., and Jirsa, V.K. (2015). Functional
584 connectivity dynamics: Modeling the switching behavior of the resting state. Neuroimage *105*,
585 525-535.

586 Harris, T.E. (1963). The Theory of Branching Processes (Berlin: Springer-Verlag).

587 Honey, C.J., Kotter, R., Breakspear, M., and Sporns, O. (2007). Network structure of cerebral
588 cortex shapes functional connectivity on multiple time scales. Proc Natl Acad Sci USA *104*,
589 10240-10245.

590 Hutchison, R.M., Womelsdorf, T., Allen, E.A., Bandettini, P.A., Calhoun, V.D., Corbetta, M.,
591 Della Penna, S., Duyn, J.H., Glover, G.H., Gonzalez-Castillo, J.*, et al.* (2013). Dynamic
592 functional connectivity: Promise, issues, and interpretations. Neuroimage *80*, 360-378.

593 Jackson, A., and Fetz, E.E. (2007). Compact movable microwire array for long-term chronic unit
594 recording in cerebral cortex of primates. J Neurophysiol *98*, 3109-3118.

595 Katzner, S., Nauhaus, I., Benucci, A., Bonin, V., Ringach, D.L., and Carandini, M. (2009). Local
596 origin of field potentials in visual cortex. Neuron *61*, 35-41.

Kinouchi, O., and Copelli, M. (2006). Optimal dynamical range of excitable networks at criticality. Nat Phys *2* 348-351.

Kirst, C., Timme, M., and Battaglia, D. (2016). Dynamic information routing in complex networks. Nature communications *7*, 11061.

Klaus, A., Yu, S., and Plenz, D. (2011). Statistical analyses support power law distributions found in neuronal avalanches. PloS one *6*, e19779.

Laurson, L., Illa, X., Santucci, S., Tore Tallakstad, K., Måløy, K.J., and Alava, M.J. (2013). Evolution of the average avalanche shape with the universality class. Nature communications *4*, 2927.

Levina, A., and Priesemann, V. (2017). Subsampling scaling. Nature communications *8*, 15140.

Li, M., Liu, F., Jiang, H., Lee, T.S., and Tang, S. (2017). Long-term two-photon imaging in awake macaque monkey. Neuron *93*, 1049-1057.e1043.

Liu, X., and Duyn, J.H. (2013). Time-varying functional network information extracted from brief instances of spontaneous brain activity. Proc Natl Acad Sci U S A *110*, 4392-4397.

Lutcke, H., Margolis, D.J., and Helmchen, F. (2013). Steady or changing? Long-term monitoring of neuronal population activity. Trends Neurosci *36*, 375-384.

Ma, Z., Turrigiano, G.G., Wessel, R., and Hengen, K.B. (2019). Cortical circuit dynamics are homeostatically tuned to criticality in vivo. Neuron *104*, 655-664.

Mehring, C., Rickert, J., Vaadia, E., Cardosa, d.O., Aertsen, A., and Rotter, S. (2003). Inference of hand movements from local field potentials in monkey motor cortex. Nat Neurosci *6*, 1253-1254.

Meisel, C., Olbrich, E., Shriki, O., and Achermann, P. (2013). Fading signatures of critical brain dynamics during sustained wakefulness in humans. J Neurosci *33*, 17363-17372.

Miller, S.R., Yu, S., and Plenz, D. (2019). The scale-invariant, temporal profile of neuronal avalanches in relation to cortical γ–oscillations. Scientific Reports *9*, 16403.

Nicolelis, M.A., Dimitrov, D., Carmena, J.M., Crist, R., Lehew, G., Kralik, J.D., and Wise, S.P. (2003). Chronic, multisite, multielectrode recordings in macaque monkeys. Proc Natl Acad Sci USA *100*, 11041-11046.

Onnela, J.P., Saramaki, J., Hyvonen, J., Szabo, G., Lazer, D., Kaski, K., Kertesz, J., and Barabási, A.L. (2007). Structure and tie strengths in mobile communication networks. Proc Natl Acad Sci USA *104*, 7332-7336.

Pajevic, S., and Plenz, D. (2009). Efficient network reconstruction from dynamical cascades identifies small-world topology from neuronal avalanches. PLoS Comp Biol *5*, e1000271.

Pajevic, S., and Plenz, D. (2012). The organization of strong links in complex networks. NatPh *8*, 429-436.

Pasquale, V., Massobrio, P., Bologna, L.L., Chiappalone, M., and Martinoia, S. (2008). Self-organization and neuronal avalanches in networks of dissociated cortical neurons. Neurosci *153*, 1354 - 1369

Petermann, T., Thiagarajan, T., Lebedev, M.A., Nicolelis, M.A., Chialvo, D.R., and Plenz, D. (2009). Spontaneous cortical activity in awake monkeys composed of neuronal avalanches. Proc Natl Acad Sci USA *106*, 15921-15926.

Plenz, D. (2012). Neuronal avalanches and coherence potentials. European Physical Journal Special Topics *205*, 259-301.

Ponce-Alvarez, A., Jouary, A., Privat, M., Deco, G., and Sumbre, G. (2018). Whole brain neuronal activtity displays crackling noise dynamics. Neuron *100*, 1446-1459.e1446.

Radicchi, F., Castellano, C., Cecconi, F., Loreto, V., and Parisi, D. (2004). Defining and identifying communities in networks. Proc Natl Acad Sci USA *101*, 2658-2663.

Raichle, M.E. (2015). The brain's default mode network. Annu Rev Neurosci *38*, 433-447.

Rasch, M.J., Gretton, A., Murayama, Y., Maass, W., and Logothetis, N.K. (2008). Inferring spike trains from local field potentials. J Neurophysiol *99*, 1461-1476.

Ribeiro, T.L., Copelli, M., Caixeta, F., Belchior, H., Chialvo, D.R., Nicolelis, M.A., and Ribeiro, S. (2010). Spike avalanches exhibit universal dynamics across the sleep-wake cycle. PloS one *5*, e14129.

650 Ribeiro, T.L., Ribeiro, S., Belchior, H., Caixeta, F., and Copelli, M. (2014). Undersampled
651 critical branching processes on small-world and random networks fail to reproduce the statistics
652 of spike avalanches. PloS one *9*, e94992.

653 Sethna, J.P., Dahmen, K.A., and Myers, C.R. (2001). Crackling noise. Nature *410*, 242-250.

654 Shew, W.L., Yang, H., Petermann, T., Roy, R., and Plenz, D. (2009). Neuronal avalanches imply
655 maximum dynamic range in cortical networks at criticality. J Neurosci *29*, 15595-15600.

656 Shew, W.L., Yang, H., Yu, S., Roy, R., and Plenz, D. (2011). Information capacity is maximized
657 in balanced cortical networks with neuronal avalanches. J Neurosci *5*, 55-63.

658 Shriki, O., Alstott, J., Carver, F., Holroyd, T., Henson, R.N., Smith, M.L., Coppola, R.,
659 Bullmore, E., and Plenz, D. (2013). Neuronal avalanches in the resting MEG of the human brain.
660 J Neurosci *33*, 7079-7090.

661 Stewart, C.V., and Plenz, D. (2007). Homeostasis of neuronal avalanches during postnatal cortex
662 development in vitro. J Neurosci Meth *169*, 405-416.

663 Tagliazucchi, E., Balenzuela, P., Fraiman, D., and Chialvo, D.R. (2012). Criticality in large-scale
664 brain fMRI dynamics unveiled by a novel point process analysis. Front Physiol *3*.

665 Tetzlaff, C., Okujeni, S., Egert, U., Wörgötter, F., and Butz, M. (2010). Self-organized criticality
666 in developing neuronal networks. PLoS Comput Biol *6*, e1001013.

667 Tolias, A.S., Ecker, A.S., Siapas, A.G., Hoenselaar, A., Keliris, G.A., and Logothetis, N.K.
668 (2007). Recording chronically from the same neurons in awake, behaving primates. J
669 Neurophysiol *98*, 3780-3790.

670 Villegas, P., Di Santo, S., Burioni, R., and Muñoz, M.A. (2019). Time-series thresholding and
671 the definition of avalanche size. Phys Rev E *100*.

672 Watts, D.J., and Strogatz, S.H. (1998). Collective dynamics of 'small-world' networks. Nature
673 *393*, 440-442.

674 Yang, H., Shew, W.L., Roy, R., and Plenz, D. (2012). Maximal variability of phase synchrony in
675 cortical networks with neuronal avalanches. J Neurosci *32*, 1061-1072.

Yu, S., Klaus, A., Yang, H., and Plenz, D. (2014). Scale-invariant neuronal avalanche dynamics and the cut-off in size distributions. PLoS One *9*, e99761.

Yu, S., Ribeiro, T.L., Meisel, C., Chou, S., Mitz, A., Saunders, R., and Plenz, D. (2017). Maintained avalanche dynamics during task-induced changes of neuronal activity in nonhuman primates. eLife *6*, e27119.

Yu, S., Yang, H., Nakahara, H., Santos, G.S., Nikolic, D., and Plenz, D. (2011). Higher-order interactions characterized in cortical activity. J Neurosci *31*, 17514-17526.

Zalesky, A., Fornito, A., Cocchi, L., Gollo, L.L., and Breakspear, M. (2014). Time-resolved resting-state brain networks. Proc Natl Acad Sci U S A *111*, 10341.